


## Article

# Three-Layered Thin Films for Simultaneous Infrared Camouflage and Radiative Cooling

Luyu Zhang <sup>1</sup>, Wenjie Zhang <sup>1,\*</sup>, Yuanbin Liu <sup>2</sup> and Linhua Liu <sup>1</sup> <sup>1</sup> School of Energy and Power Engineering, Shandong University, Jinan 250061, China<sup>2</sup> Key Laboratory for Thermal Science and Power Engineering of Ministry of Education, Department of Engineering Mechanics, Tsinghua University, Beijing 100084, China

\* Correspondence: zhangwenjie@sdu.edu.cn

**Abstract:** With the rapid advancements in aerospace technology and infrared detection technology, there are increasing needs for materials with simultaneous infrared camouflage and radiative cooling capabilities. In this study, a three-layered Ge/Ag/Si thin film structure on a titanium alloy TC4 substrate (a widely used skin material for spacecraft) is designed and optimized to achieve such spectral compatibility by combining the transfer matrix method and the genetic algorithm. The structure exhibits a low average emissivity of 0.11 in the atmospheric windows of 3–5  $\mu\text{m}$  and 8–14  $\mu\text{m}$  for infrared camouflage and a high average emissivity of 0.69 in 5–8  $\mu\text{m}$  for radiative cooling. Furthermore, the designed metasurface shows a high degree of robustness regarding the polarization and incidence angle of the incoming electromagnetic wave. The underlying mechanisms allowing for the spectral compatibility of the metasurface can be elucidated as follows: the top Ge layer selectively transmits electromagnetic waves ranging from 5–8  $\mu\text{m}$  while it reflects those in the ranges of 3–5  $\mu\text{m}$  and 8–14  $\mu\text{m}$ . The transmitted electromagnetic waves from the Ge layer are first absorbed by the Ag layer and then localized in the Fabry-Perot resonance cavity formed by Ag layer, Si layer and TC4 substrate. Ag and TC4 make further intrinsic absorptions during the multiple reflections of the localized electromagnetic waves.

**Keywords:** multilayered thin films; infrared camouflage; radiative cooling; Fabry-Perot resonance cavity



**Citation:** Zhang, L.; Zhang, W.; Liu, Y.; Liu, L. Three-Layered Thin Films for Simultaneous Infrared Camouflage and Radiative Cooling. *Materials* **2023**, *16*, 4188. <https://doi.org/10.3390/ma16114188>

Academic Editor: Frank Czerwinski

Received: 3 April 2023

Revised: 30 May 2023

Accepted: 3 June 2023

Published: 5 June 2023



**Copyright:** © 2023 by the authors. Licensee MDPI, Basel, Switzerland. This article is an open access article distributed under the terms and conditions of the Creative Commons Attribution (CC BY) license (<https://creativecommons.org/licenses/by/4.0/>).

## 1. Introduction

With the rapid development of the aerospace industry, the infrared (IR) camouflage of spacecraft is attracting more and more research attention [1]. Full IR band (from near infrared to far infrared) low emissivity coatings have been commonly used in IR camouflage for years, although the IR radiation signals of spacecraft mainly depend on its temperature-dependent emissivity being within the mid-far IR atmospheric windows (3–5  $\mu\text{m}$  and 8–14  $\mu\text{m}$ ) [2]. In this regard, the low emissivity of 5–8  $\mu\text{m}$  significantly hinders the radiative cooling efficiency of a spacecraft, which may raise the temperature level and largely limit its camouflage performance. Hence, high performance IR camouflage coating demands favorable spectral selectivity, i.e., high emissivity in non-atmospheric window bands for radiative cooling [3] and low emissivity in the atmospheric window bands for IR camouflage [4].

Recently, multilayered thin films have emerged that efficiently tune the radiative properties of materials [5–11]. As a type of metamaterial, multilayered thin films are composed of two or more stack-arranged dielectric materials, which have great potential for applications in perfect absorbers (PAs) [5,11–14], radiative cooling [15–19] and IR camouflage [20–28]. While the investigation of individual functionalities is progressively advancing, the exploration of multilayered thin films that can be compatible with diverse functionalities is thriving. For example, Qi et al. [29] designed a one-dimensional photonic crystal structure based on ZnS/Ge to achieve visible and infrared compatible stealth.

Deng et al. [30] proposed a low visibility and low thermal emission thin film structure for multispectral camouflage. Kang et al. [31] designed a plasma structure based on  $\text{Ge}_2\text{Sb}_2\text{Te}_5$  (GST) for tunable multi-band camouflage and radiative cooling. Zhao et al. [21] realized broad-spectrum infrared spectral selectivity through a 20-layered and a 23-layered thin film structure. Wang et al. [32] designed an IR camouflage-radiative cooling compatible structure consisting of 12 layers of thin film. Considering the structural simplicity for large-scale fabrication, Liang et al. [33] and Yang et al. [34] proposed a four-layered film structure to achieve the compatibility of IR camouflage and thermal management. Zhu et al. [35] and Pan et al. [36] achieved laser camouflage and visual camouflage alongside the compatibility of IR camouflage and radiative cooling by combining multilayered structures and surface microstructures, respectively. However, in most of the previous works, the structural parameters of the multilayered thin films were not rigorously optimized, while the polarization and incidence angle robustness of the structure were rarely included. Moreover, multilayered thin film structures with compatibility of IR camouflage and radiative cooling using fewer layers are highly desirable to further decrease the difficulties of large-scale fabrication. In addition, for a more comprehensive overview of the previously reported designs' functionality and structure in various scenarios, we present a summary in Table 1.

**Table 1.** Comparison of representative theoretical and experimental works on thermal camouflage compatibility in recent years.

Work by	Multilayered Films Only	Number of Layers	3–5 $\mu\text{m}$ Infrared Camouflage	5–8 $\mu\text{m}$ Radiative Cooling	8–14 $\mu\text{m}$ Infrared Camouflage
Qi et al. [29]	✓	8	✓	×	×
Deng et al. [30]	✓	6	✓	×	✓
Kang et al. [31]	×	×	✓	✓	✓
Zhao et al. [21]	✓	20/23	×	✓	✓
Wang et al. [32]	✓	12	✓	✓	✓
Liang [33] and Yang [34] et al.	✓	4	✓	✓	✓
Zhu [35] and Pan [36] et al.	×	×	✓	✓	✓

“✓” and “×” denote “yes” and “no”, respectively.

This work proposes a three-layered Ge/Ag/Si thin film structure on a TC4 substrate for spectrally selective modulation to achieve compatibility with IR camouflage and radiative cooling. The material and thickness of each layer are optimized via a genetic algorithm (GA) [37–40], a powerful optimization method used for structural parameters that simulates the processes of inheritance and variation in biological populations. The final structure exhibits broad-spectrum low emissivity for IR camouflage in the atmospheric windows of 3–5  $\mu\text{m}$  and 8–14  $\mu\text{m}$ , and broad-spectrum high emissivity for radiative cooling in the non-atmospheric windows of 5–8  $\mu\text{m}$ . Furthermore, the directional performance for different polarizations and the underlying mechanisms are discussed in detail. The results demonstrate that the compatibility can be maintained over a wide directional range of  $0^\circ$  to  $80^\circ$  and is insensitive to the polarization state.

## 2. Methodology

### 2.1. Design Process

The schematic and design strategy of the multilayered thin films are illustrated in Figure 1. The structure is composed of  $n$  unit layers. The material and thickness of each layer are denoted as  $m_i$  and  $d_i$ , respectively. In principle, they are expected to achieve the spectral selectivity by combining the unique electromagnetic response of each stacked layer: (1) the top layers allow transmission in the non-atmospheric window band but reflect in the atmospheric window band; (2) the inner layers absorb the transmitted electromagnetic waves in the non-atmospheric window band. In the design process, the transfer matrix

method (TMM) and the GA are combined to determine the optimized layer number  $n$ , the material  $m_i$  and the thickness  $d_i$  of each layer. Specifically, the GA is used for the structural parameters optimizing iterations, while the TMM is used to calculate the apparent emissivity in each iteration. The essentials of TMM and GA are presented below.

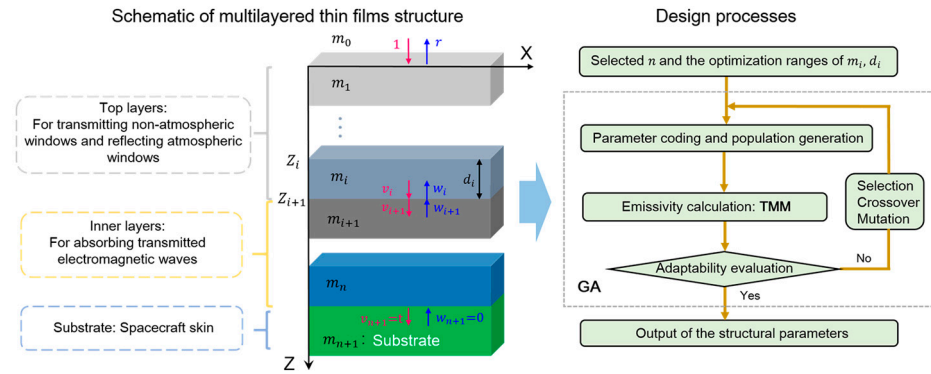


Figure 1. Schematic of the model and method for the design of multilayered thin films.

### 2.2. Emissivity Calculation for Multilayered Thin Films

The TMM is an accurate and efficient method used to calculate the reflectance and transmittance of multilayered thin films [41]. The TMM describes the forward and backward amplitude change in each film layer and at its boundaries via transfer matrix. For the structure shown in Figure 1, light with a normalized electric field amplitude of 1 passes through the  $n$  isotropic film layers from a vacuum (layer 0) to the substrate (layer  $n + 1$ ). If we denote the forward and backward amplitude on the  $i$ th side by  $v_i$  and  $w_i$ , respectively, there are relationships between them [42]:

$$v_{i+1} = (v_i e^{i\delta_i}) t_{i,i+1} + w_{i+1} r_{i+1,i} \tag{1}$$

$$w_i e^{-i\delta_i} = w_{i+1} t_{i+1,i} + (v_i e^{i\delta_i}) r_{i,i+1} \tag{2}$$

where  $r_{a,b}$  and  $t_{a,b}$  denote the reflection and transmission coefficient from layer  $a$  to its adjacent layer  $b$ , respectively.  $a$  and  $b$  represent the layer number, like  $i$  or  $i + 1$ .  $\delta_i$  is the phase change passing through the  $i$ th layer, and is expressed as [42]:

$$\delta_i = d_i \cdot k_{z,i} \tag{3}$$

$k_{z,i}$  denotes the normal components of the complex wave vector in the  $i$ th layer [42]:

$$k_{z,i} = \frac{2\pi}{\lambda} \tilde{n}_i(\lambda) \cos(\theta_i) \tag{4}$$

where  $\tilde{n}_i$  and  $\theta_i$  represent the complex refractive index and the incident angle of the  $i$ th layer, respectively, while  $\lambda$  represents the wavelength.

Next, the amplitude change in each layer ( $i = 1, \dots, n - 1$ ) can be expressed by the layer transfer matrix  $M_i$  in the form [42]:

$$\begin{pmatrix} v_i \\ w_i \end{pmatrix} = M_i \begin{pmatrix} v_{i+1} \\ w_{i+1} \end{pmatrix} = \begin{bmatrix} e^{-i\delta_i} & 0 \\ 0 & e^{i\delta_i} \end{bmatrix} \begin{pmatrix} 1 & r_{i,i+1} \\ r_{i,i+1} & 1 \end{pmatrix} \frac{1}{t_{i,i+1}} \begin{pmatrix} v_{i+1} \\ w_{i+1} \end{pmatrix} \tag{5}$$

The consequent amplitude change can be expressed by the total transfer matrix  $\tilde{M}$  connecting each layer [42]:

$$\begin{pmatrix} 1 \\ r \end{pmatrix} = \tilde{M} \begin{pmatrix} t \\ 0 \end{pmatrix} \tag{6}$$

$$\tilde{M} = \frac{1}{t_{0,1}} \begin{pmatrix} 1 & r_{0,1} \\ r_{0,1} & 1 \end{pmatrix} M_1 M_1 \cdots M_{n-1} \quad (7)$$

The reflectivity and transmissivity can be obtained by [42]:

$$R = |r|^2 = \left| 1/\tilde{M}_{11} \right|^2, T = |t|^2 = \left| \tilde{M}_{21}/\tilde{M}_{11} \right|^2 \quad (8)$$

When the reflectance  $R$  and the transmittance  $T$  are calculated, their corresponding absorbance  $\alpha = 1 - T - R$  can also be calculated. In this study, the titanium alloy TC4 spacecraft skin is taken as the substrate, such that the transmittance of the structure is  $t = 0$ . Then the absorbance can be approximated as  $\alpha = 1 - R$ . From Kirchhoff's law, it is known that the absorbance is equal to the emissivity at thermal equilibrium, i.e.,  $\varepsilon = \alpha$ . In this study, we use the open-source program TMM to calculate the absorptivity and reflectivity of the multilayer film structure [43].

### 2.3. Genetic Algorithm

The GA is a biomimetic optimization method that simulates the phenomena of selection, crossover and mutation in biological genetics. The GA starts with a random initial population and iteratively generates individuals better suited to the environment through the manipulation of genetic operators. Eventually, the population evolves into an optimal solution within the defined parameter range [33,34]. Semi-conductor materials Ge and Si exhibit a stable high refractive index and near-zero extinction coefficients, while noble metal materials Ag and Pt exhibit a monotonically increasing high refractive index ( $n$ ) and extinction coefficients ( $k$ ) with wavelength in the 3–14  $\mu\text{m}$  band. The infrared optical constants ( $n, k$ ) for Ge [44], Si [45], Ag [46], and Pt [47] materials within the 3–14  $\mu\text{m}$  band are depicted in Figure 2. The strategic combination of these materials, with specific thicknesses, has been demonstrated in the literature to possess superior selectively emissive characteristics [33,34]. Here, in order to realize the original design intention, i. e. achieving the spectral selectivity by combining different electromagnetic responses of the top layers, inner layers and the bottom layers, we take Ge, Si, Ag, and Pt as the candidate materials for the stacked structure, and encode the material of each layer as  $m_i$ .

For practical engineering applications, the simplicity of large-scale fabrication is a critical factor, to which intensive attention should be paid. In order to achieve the original design intention with as few layers as possible, the number of top layers, inner layers, and bottom layers are all set to  $n = 1$ . Namely, the total layer number is  $n = 3$ . The candidate material of each layer is configured as: the first layer uses Ge or Si for the spectrally selective transmission of the incident light; the second layer uses the ultrathin metal layer Ag or Pt for absorption of the light transmitted from the first layer; the third layer uses Ge or Si for the resonance with the second thin metal layer to further enhance the absorption of the light transmitted from the second layer. The material of each layer will be determined throughout the GA optimization process. Alongside the candidate material  $m_i$ , the thickness  $d_i$  is the other key parameter affecting the apparent emissivity of the multilayered thin film structure. To avoid possible local optimum values, eight structures composed of different materials are evolved and screened with three genes per layer thickness  $d_i$  as an individual.

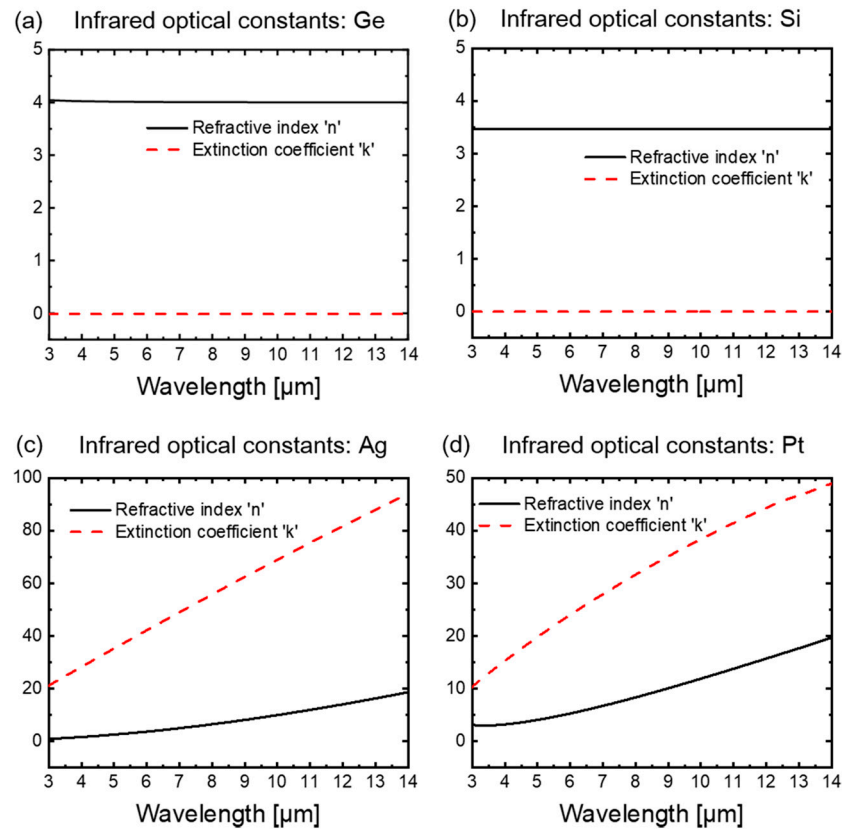


**Figure 2.** Infrared optical constants ( $n$ ,  $k$ ) of (a) Ge, (b) Si, (c) Ag, (d) Pt in the 3–14 μm range.

The optimization process begins by generating a population with different parameter combinations within the defined range, then the spectral emissivity levels in 3–14 μm of each individual combination are calculated by the TMM. Since IR detection and radiative cooling concerns integrated radiation power in certain spectral range, the adaptability of each individual with gene  $D = [d_1, d_2, d_3]$  is evaluated through the objective function based on spectrally integrated average emissivity:

$$f(D) = \sqrt{\frac{\sum_{j=1}^3 g_j [\varepsilon_{tar}(j) - \varepsilon_{cal}(j)]^2}{3}} \quad (9)$$

where  $\varepsilon_{tar}$  and  $\varepsilon_{cal}$  represent the expected and calculated average emissivity, respectively.  $j = 1, 2, 3$  denotes the three concerning bands, i.e., the mid-IR atmosphere window 3–5 μm, the radiative cooling band 5–8 μm, and the far-IR atmosphere window 8–14 μm, respectively.  $g_j$  is the weight factor corresponding to the concerning bands, and the band with a relatively large weight factor will be especially focused on in the evaluation. Towards the IR camouflage and radiative cooling compatibility, the expected average emissivity in 3–5 μm, 5–8 μm and 8–14 μm are set to [0 1 0] and the weighting factor is set to [1 1 1], respectively. In each generation, good genes will be selected referring to low objective function values of the population, while the bad genes will be mutated. The selected good genes crossover and become the next generation of the initial population. The objective value continuously decreases with the iterative evolution process of the population. Convergence will be achieved when the relative difference of the objective value between two adjacent generations is smaller than  $10^{-4}$  in this study:

$$F = |f_{\beta+1}(D) - f_{\beta}(D)| / f_{\beta}(D) < 10^{-4} \quad (10)$$

where  $\beta$  and  $\beta + 1$  represent two adjacent generations. Eventually, the optimized results are obtained. In this study, the number of individuals in the random population is set to 40, and the maximum number of genetic generations is set to 25. The thickness range of each layer is set to 0.01–1  $\mu\text{m}$ . Figure 3 illustrates the evolution of the objective function in the GA for one set of layered films. For all eight sets of structures, the GA achieves convergence within 25 generations.

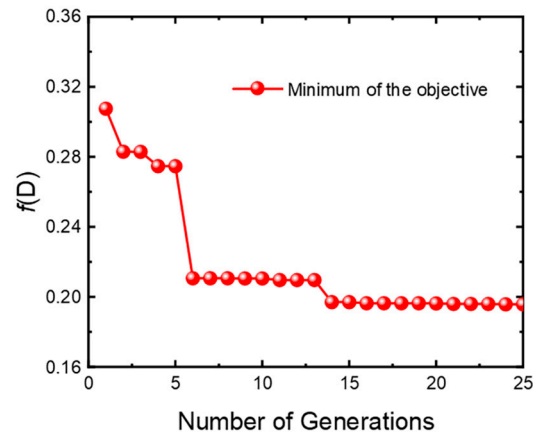


**Figure 3.** Evolution of the best objective value in the optimization for one set of layered films.

### 3. Results and Discussion

The final optimized structural parameters are shown in Table 2. The structure includes a Ge film layer, an ultra-thin Ag film layer, and a Si film layer with a thickness of 333 nm, 10 nm, and 760 nm, respectively. The three layers are stacked on the TC4 titanium alloy substrate. In order to evaluate the radiative properties of the structure optimized by the GA, we calculated the normal spectral emissivity and reflectivity, as shown in Figure 4. The shaded area in the figure is the transmittance of the atmospheric window. It is shown that the optimized structure has broad-spectrum low emissivity in the 3–5  $\mu\text{m}$  and 8–14  $\mu\text{m}$  atmospheric window bands as well as broad-spectrum high emissivity in the 5–8  $\mu\text{m}$  non-atmospheric window band. We further calculated the average emissivity of these target bands as  $\epsilon_{\text{avg},3-5 \mu\text{m}} = 0.11$ ,  $\epsilon_{\text{avg},8-14 \mu\text{m}} = 0.11$ ,  $\epsilon_{\text{avg},5-8 \mu\text{m}} = 0.69$ , respectively. The results demonstrate that the optimized structure has desirable infrared camouflage and radiative cooling compatibility.

**Table 2.** The optimized parameters of the compatible multilayered thin films structure.

	Layer 1	Layer 2	Layer 3	Substrate
Material	Ge	Ag	Si	TC4
Thickness/[nm]	333	10	760	/

Emission direction and polarization characteristics are two more important factors in IR camouflage performance. Hence, we further examined the polarization and directional robustness of the optimized structure via the TMM. The spectral absorptivity of both  $p$ - and  $s$ - polarizations at different incidence angles are shown in Figure 5. It is shown that, for both  $p$ - and  $s$ - polarizations, the structure exhibits high absorptivity for non-atmospheric windows and low absorptivity for atmospheric windows over a wide angular range (0–80°). Since all of the thin films and the substrate are isotropic materials, according to Kirchhoff's law, the emissivity of the optimized structure can be obtained by averaging the  $s$ - and  $p$ -polarized absorptivity, as shown in Figure 6. The results indicate that the infrared camouflage and radiative cooling compatibility of the coating is insensitive to direction and polarization.

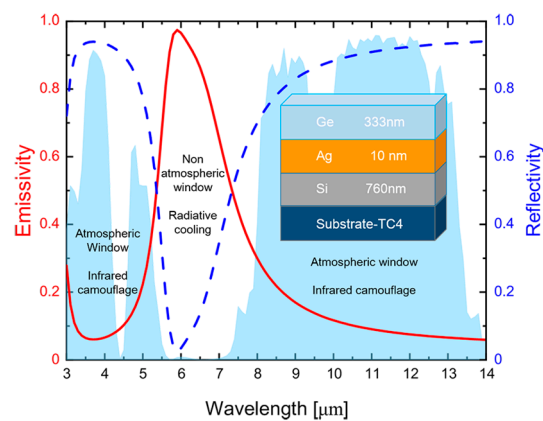


**Figure 4.** Spectral emissivity (red solid line) and reflectivity (blue dashed line) of the optimized multi-layered thin films. For convenience, the optimized structure is shown in the inset, in which the selected materials and thicknesses are also labeled. The shaded area represents the atmospheric transmittance.

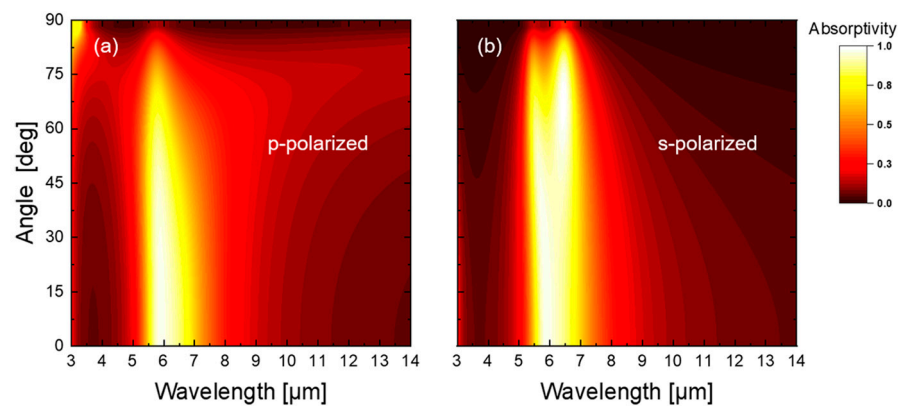


**Figure 5.** Polarized absorptivity of the optimized structure at different angles (a) *p*-polarized (b) *s*-polarized.

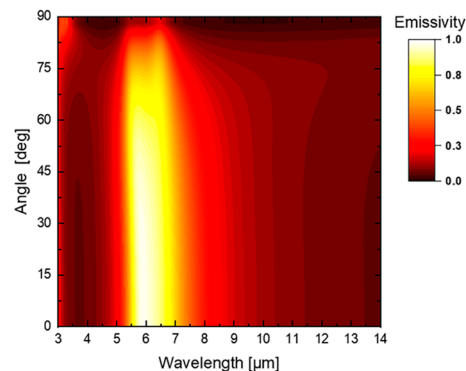


**Figure 6.** Emissivity of the optimized structure at different angles.

In order to access the radiative cooling performance and camouflage performance of the three-layered film structure, we calculated the emissive power density in 5–8  $\mu\text{m}$  for radiative cooling and the IR radiation signal power density in 3–5  $\mu\text{m}$  and 8–14  $\mu\text{m}$  for being detected by Equation (11) [31], respectively, where  $\lambda_1$  and  $\lambda_2$  are the minimum and maximum wavelengths of the integral spectra range, as shown in Figure 7. It can be observed that the radiative cooling power density increases significantly while the IR radiation signal power densities increase slightly with increasing temperature from 300 K to 900 K. Moreover, the remarkable increase of the radiative cooling power will contribute to the reduction of the spacecraft surface temperature, thus further suppressing the increase of

the IR radiation signal intensity in the 3–5  $\mu\text{m}$  and 8–14  $\mu\text{m}$  detection bands. Consequently, the structure exhibits excellent compatible camouflage and radiative cooling performance, especially for high temperature spacecraft. In addition, the structure designed in this study achieves this compatibility with only three layers, which is simpler and more easily fabricated than those listed in Table 1.

$$E_{\lambda_1-\lambda_2}(T) = \int_{\lambda_1}^{\lambda_2} \varepsilon(\lambda) E_b(\lambda, T) d\lambda \quad (11)$$

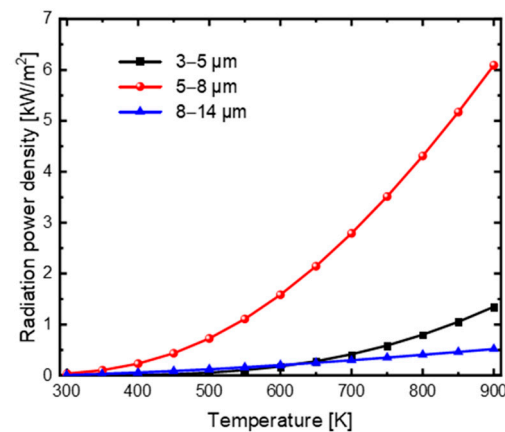


**Figure 7.** The emissive power density in 5–8  $\mu\text{m}$  for radiative cooling, and the IR radiation signal power density in the detection bands of 3–5  $\mu\text{m}$  and 8–14  $\mu\text{m}$ .

In order to clarify the mechanism of the spectrally selective emissivity, we examined the normalized electric field of the optimized structure at wavelengths of 4  $\mu\text{m}$  and 11  $\mu\text{m}$  in the atmospheric window and at wavelengths of 6  $\mu\text{m}$  and 7  $\mu\text{m}$  in the non-atmospheric window as examples, respectively, as shown in Figure 8. It can be seen that the electric field intensity of the structure at wavelengths of 4  $\mu\text{m}$  and 11  $\mu\text{m}$  are much lower than that at wavelengths of 6  $\mu\text{m}$  and 7  $\mu\text{m}$ , which indicates that the outer surface of the top Ge layer makes the first spectral selection. That is, the top Ge layer reflects off most of the electromagnetic waves in the atmospheric window bands (see 4  $\mu\text{m}$  and 11  $\mu\text{m}$ ) but allows the electromagnetic waves in the non-atmospheric window band (see 6  $\mu\text{m}$  and 7  $\mu\text{m}$ ) to penetrate into the interior of the stacked structure. Once the electromagnetic waves within the non-atmospheric window enter the interior of the structure, they are first attenuated during their passage through the top Ge layer, and subsequently the remaining waves propagate onto the ultra-thin Ag layer. The Ag layer plays a key role in two aspects. One aspect is that the thin Ag layer forms the Fabry-Perot (F-P) resonance [48] together with the Si layer and the titanium alloy substrate. The F-P resonance localizes the electromagnetic waves in the cavity. The other aspect is that the thin Ag layer can efficiently absorb both the localized electromagnetic waves and the transmitted electromagnetic waves from the Ge layer. Figure 9 illustrates the absorption distribution of the optimized structure at 6  $\mu\text{m}$  and 7  $\mu\text{m}$  under normal incidence, where the power absorption density ( $\text{W}/\text{m}^3$ ) is defined as [49,50]:

$$w(x, y, z) = \frac{1}{2} \varepsilon_0 \omega \varepsilon''(x, y, z) |E(x, y, z)|^2 \quad (12)$$

where  $\varepsilon_0$  and  $\varepsilon''$  denote the permittivity of vacuum and the imaginary part of the dielectric function of the stacked layers, respectively.  $\omega$  represents the angular frequency, and  $E$  is the electric field vector. It is shown that, alongside the Ag layer, the titanium alloy substrate can further absorb the localized waves in the F-P resonance cavity.



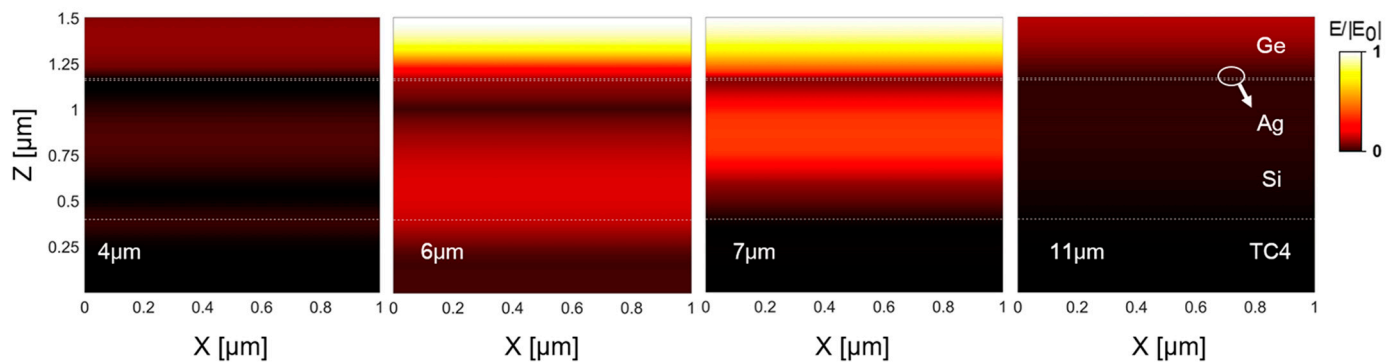


**Figure 8.** The internal normalized electric field distribution of the optimized structure at the wavelengths of 4  $\mu\text{m}$ , 6  $\mu\text{m}$ , 7  $\mu\text{m}$ , and 11  $\mu\text{m}$ . The white dash lines denote the interfaces between the layers, and the white circle indicates the ultrathin Ag layer.

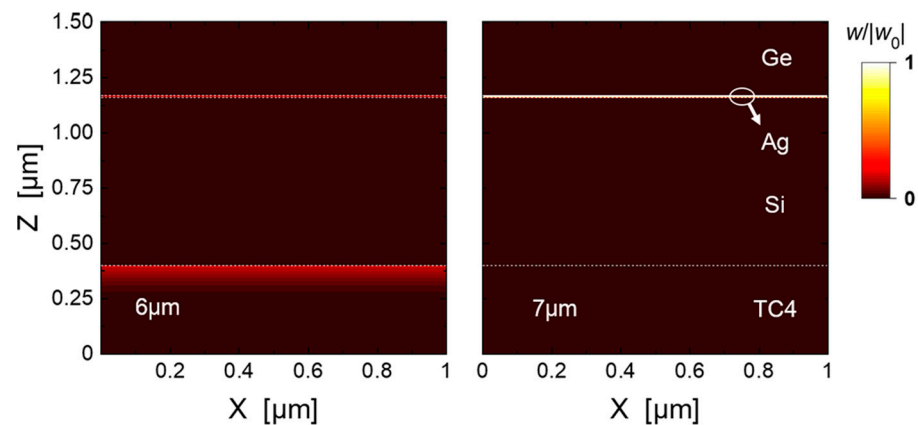


**Figure 9.** Normalized absorption distribution of the optimized structure at the wavelengths of 6  $\mu\text{m}$  and 7  $\mu\text{m}$ .

Figure 10 illustrates the spectral absorption distribution in the entire 3–14  $\mu\text{m}$  band. It can be seen that the greatly enhanced absorption mainly focuses on the thin Ag layer in 6–8  $\mu\text{m}$ , and a weaker absorption occurs in the TC4 substrate in 5–6  $\mu\text{m}$ . The combination of the absorption by the Ag layer and the TC4 substrate leads to the apparent high emissivity of the optimized structure in the 5–8  $\mu\text{m}$  non-atmosphere window for radiative cooling. Although the top Ge layer also absorbs within this band, the power absorption density is much lower than the Ag layer and the substrate. In addition, the absorption density in the 3–5  $\mu\text{m}$  and 8–14  $\mu\text{m}$  ranges is much lower than that in the 5–8  $\mu\text{m}$  range, which is the reason for the low emissivity in the atmospheric window bands. Consequently, it is verified that the optimized structure realizes the IR camouflage and radiative cooling compatibility with the electromagnetic response combination of each layer. In this study, we used the open-source software S4 (version 1.1.1) [51] to calculate the internal normalized electric field distribution and normalized absorption distribution in the optimized structure.

Considering the uncertainties in the fabrication process, the film thickness of each layer of the samples or products will deviate from the optimized value, so that the apparent spectral emissivity of the structure will be influenced. In order to quantitatively evaluate the thickness sensitivity, we calculate the apparent spectral emissivity of the three-layered film structure for varying thickness of each layer with the single variable principle, respectively. The results are illustrated in Figure 11, where the white dashed lines represent the desired thicknesses optimized by the GA. It can be seen from Figure 11 that the apparent spectral emissivity remains nearly unchanged within a Ge/Si layer thickness variation range of approximately  $\pm 20$  nm while it changes remarkably within the Ag layer thickness variation range of only approximately  $\pm 10$  nm. The sensitivity difference between Ge/Si layer

thickness and Ag layer thickness can be attributed to the different roles of each layer. Since the Ag layer simultaneously plays the roles of both forming the F-P resonance cavity and absorbing the transmitted electromagnetic waves from the Ge layer and localized electromagnetic waves in the F-P resonance cavity, its thickness becomes the key factor affecting the apparent spectral emissivity of the structure. Hence, the thickness of Ag layer should be specially and accurately controlled in the manufacturing process.

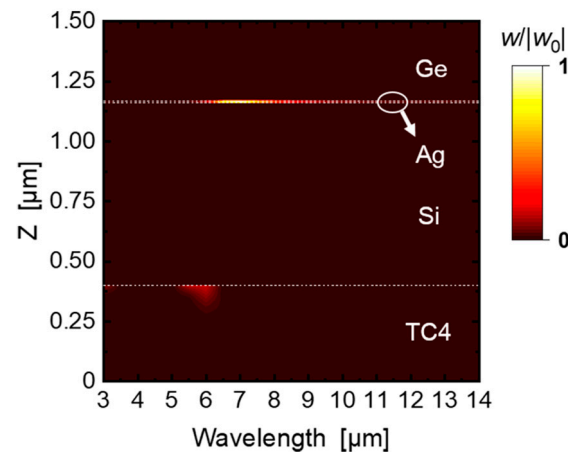


**Figure 10.** Normalized spectral absorption distribution of the optimized structure.

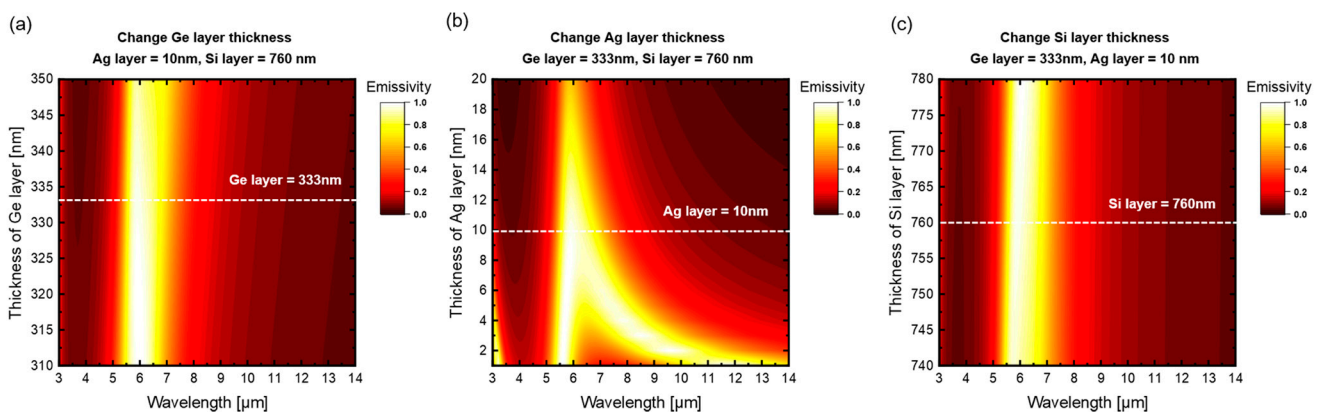


**Figure 11.** Sensitivity of the spectral emissivity to the thickness of each layer: (a) Ge layer, (b) Ag layer, (c) Si layer. The white dashed lines represent the desired thicknesses optimized by GA.

#### 4. Conclusions

In order to achieve compatible infrared camouflage and radiative cooling for spacecraft, a three-layered Ge/Ag/Si thin film structure on a TC4 substrate is designed via a GA and a TMM. The optimized structure can realize broad-spectrum low emissivity of 0.11 in the 3–5  $\mu\text{m}$  and 8–14  $\mu\text{m}$  atmospheric window bands for IR camouflage, and high average emissivity of over 0.69 in the 5–8  $\mu\text{m}$  non-atmospheric window bands for radiative cooling. By calculating the radiative cooling power density and the IR radiation signal power density, we demonstrate the excellent camouflage and cooling compatibilities of the optimized structure, especially for high temperature spacecraft. Moreover, this compatibility can be maintained over a wide directional range of 0–80° for different polarizations. The mechanism analysis demonstrates that the compatibility can be attributed to the spectral selectivity of the top Ge layer, the intrinsic absorption of the inner Ag layer, and the excitation of the Fabry-Perot resonance formed by Ag, Si and TC4 substrate. The optimized structure achieves the compatibility of radiative cooling and IR camouflage with only three layer films, which is expected to be more applicable for large-scale fabrication and practical engineering applications.

**Author Contributions:** Conceptualization, L.L.; methodology, W.Z.; validation, L.Z. and W.Z.; formal analysis, L.Z., W.Z. and Y.L.; investigation, L.Z.; resources, L.Z.; writing—original draft preparation, L.Z.; writing—review and editing, Y.L. and L.L.; supervision, W.Z.; funding acquisition, W.Z. All authors have read and agreed to the published version of the manuscript.

**Funding:** This research was funded by the National Natural Science Foundation of China (52006127) and the Natural Science Foundation of Shandong Province (ZR2020QE194).

**Institutional Review Board Statement:** Not applicable.

**Informed Consent Statement:** Not applicable.

**Data Availability Statement:** The data that support the findings of this study are available from the corresponding author upon reasonable request.

**Conflicts of Interest:** The authors declare no conflict of interest.

## References

1. Zhu, H.; Li, Q.; Zheng, C.; Hong, Y.; Xu, Z.; Wang, H.; Shen, W.; Kaur, S.; Ghosh, P.; Qiu, M. High-temperature infrared camouflage with efficient thermal management. *Light-Sci. Appl.* **2020**, *9*, 60. [[CrossRef](#)] [[PubMed](#)]
2. Ding, P.; Wang, P.; Su, J.; Mao, B.; Ren, M.; Xu, K.; Tian, S.; Li, Y.; Tian, X.; Wang, J. Multilayer graphene-based radiation modulator for adaptive infrared camouflage with thermal management. *J. Phys. D Appl. Phys.* **2022**, *55*, 345103. [[CrossRef](#)]
3. Kang, Q.; Li, D.; Guo, K.; Gao, J.; Guo, Z. Tunable thermal camouflage based on GST plasmonic metamaterial. *Nanomaterials* **2021**, *11*, 260. [[CrossRef](#)] [[PubMed](#)]
4. Huang, Y.J.; Pu, M.B.; Zhao, Z.Y.; Li, X.; Ma, X.L.; Luo, X.G. Broadband metamaterial as an “Invisible” radiative cooling coat. *Opt. Commun.* **2018**, *407*, 204–207. [[CrossRef](#)]
5. Yang, C.; Ji, C.; Shen, W.; Lee, K.-T.; Zhang, Y.; Liu, X.; Guo, L.J. Compact multilayer film structures for ultrabroadband, omnidirectional, and efficient absorption. *ACS Photonics* **2016**, *3*, 590–596. [[CrossRef](#)]
6. Kumar, C.A.; Anurag, R.V.; Debabrata, S. Selective thermal emitters for high-performance all-day radiative cooling. *J. Phys. D Appl. Phys.* **2021**, *55*, 085504.
7. Yao, Y.; Liao, Z.; Liu, Z.; Liu, X.; Zhou, J.; Liu, G.; Yi, Z. Recent progresses on metamaterials for optical absorption and sensing: A review. *J. Phys. D Appl. Phys.* **2021**, *54*, 113002. [[CrossRef](#)]
8. Ali, A.; Mitra, A. Metamaterials and metasurfaces: A review from the perspectives of materials, mechanisms and advanced metadevices. *Nanomaterials* **2022**, *12*, 1027. [[CrossRef](#)]
9. Boriskina, S.V.; Tong, J.K.; Huang, Y.; Zhou, J.; Chiloyan, V.; Chen, G. Enhancement and tunability of near-field radiative heat transfer mediated by surface plasmon polaritons in thin plasmonic films. *Photonics* **2015**, *2*, 659–683. [[CrossRef](#)]
10. Liu, Y.; Bai, A.; Fang, Z.; Ni, Y.; Lu, C.; Xu, Z. A pragmatic bilayer selective emitter for efficient radiative cooling under direct sunlight. *Materials* **2019**, *12*, 1208. [[CrossRef](#)]
11. Streyer, W.; Law, S.; Rooney, G.; Jacobs, T.; Wasserman, D. Strong absorption and selective emission from engineered metals with dielectric coatings. *Opt. Express* **2013**, *21*, 9113–9122. [[CrossRef](#)] [[PubMed](#)]
12. Cai, H.; Wang, M.; Wu, Z.; Wang, X.; Liu, J. Design of multilayer planar film structures for near-perfect absorption in the visible to near-infrared. *Opt. Express* **2022**, *30*, 35219–35231. [[CrossRef](#)] [[PubMed](#)]
13. Kim, T.Y.; Badsha, M.A.; Yoon, J.; Lee, S.Y.; Jun, Y.; Hwangbo, C. General strategy for broadband coherent perfect absorption and multi-wavelength all-optical switching based on epsilon-near-zero multilayer films. *Sci. Rep.* **2016**, *6*, 22941. [[CrossRef](#)] [[PubMed](#)]
14. Liang, C.; Yi, Z.; Chen, X.; Tang, Y.; Yi, Y.; Zhou, Z.; Wu, X.; Huang, Z.; Yi, Y.; Zhang, G. Dual-Band infrared perfect absorber based on a Ag-Dielectric-Ag multilayer films with nanoring grooves arrays. *Plasmonics* **2019**, *15*, 93–100. [[CrossRef](#)]
15. Raman, A.P.; Anoma, M.A.; Zhu, L.; Rephaeli, E.; Fan, S. Passive radiative cooling below ambient air temperature under direct sunlight. *Nature* **2014**, *515*, 540–544. [[CrossRef](#)]
16. Eden, R.; Aaswath, R.; Shanhuai, F. Ultrabroadband photonic structures to achieve high-performance daytime radiative cooling. *Nano Lett.* **2013**, *13*, 1457–1461.
17. Huang, Z.; Ruan, X. Nanoparticle embedded double-layer coating for daytime radiative cooling. *Int. J. Heat Mass Transf.* **2017**, *104*, 890–896. [[CrossRef](#)]
18. Naghshine, B.B.; Saboonchi, A. Optimized thin film coatings for passive radiative cooling applications. *Opt. Commun.* **2018**, *410*, 416–423. [[CrossRef](#)]
19. Wu, D.; Liu, C.; Xu, Z.; Liu, Y.; Yu, Z.; Yu, L.; Chen, L.; Li, R.; Ma, R.; Ye, H. The design of ultra-broadband selective near-perfect absorber based on photonic structures to achieve near-ideal daytime radiative cooling. *Mater. Des.* **2018**, *139*, 104–111. [[CrossRef](#)]
20. Lee, N.; Kim, T.; Lim, J.S.; Chang, I.; Cho, H.H. Metamaterial-selective emitter for maximizing infrared camouflage performance with energy dissipation. *ACS Appl. Mater. Interfaces* **2019**, *11*, 21250–21257. [[CrossRef](#)]

21. Zhao, Z.; Li, G.; Su, T.; Yu, F.; Zhang, Y.; Wang, W.; Men, W.; Wang, Z.; Xuan, L.; Chen, X.; et al. Selectively thermal radiation control in long-wavelength infrared with broadband all-dielectric absorber. *Opt. Express* **2019**, *27*, 35088–35095. [[CrossRef](#)] [[PubMed](#)]
22. Zhao, L.; Liu, H.; He, Z. All-metal frequency-selective absorber/emitter for laser stealth and infrared stealth. *Appl. Opt.* **2018**, *57*, 1757–1764. [[CrossRef](#)]
23. Changhoon, P.; Jagyeong, K.; Hahn, J.W. Selective emitter with engineered anisotropic radiation to minimize dual-band thermal signature for infrared stealth technology. *ACS Appl. Mater. Interfaces* **2020**, *12*, 43090–43097.
24. Zhong, S.; Wu, L.; Liu, T.; Huang, J.; Jiang, W.; Ma, Y. Transparent transmission-selective radar-infrared bi-stealth structure. *Opt. Express* **2018**, *26*, 16466–16476. [[CrossRef](#)] [[PubMed](#)]
25. Kim, J.; Han, K. Selective dual-band metamaterial perfect absorber for infrared stealth technology. *Sci. Rep.* **2017**, *7*, 6740. [[CrossRef](#)] [[PubMed](#)]
26. Xiao, C.; Chang, T.; Zhi, C.; Tian, C. Selective metamaterial perfect absorber for infrared and 1.54  $\mu\text{m}$  laser compatible stealth technology. *Optik* **2018**, *172*, 840–846.
27. Zhao, J.; Zhou, B.; Wang, G.; Ying, J.; Liu, J.; Chen, Q. Spectral camouflage characteristics and recognition ability of targets based on visible/near-infrared hyperspectral images. *Photonics* **2022**, *9*, 957. [[CrossRef](#)]
28. Wang, L.; Fu, Q.; Wen, F.; Zhou, X.; Ding, X.; Wang, Y. A thermally controlled multifunctional metamaterial absorber with switchable wideband absorption and transmission at THz band. *Materials* **2023**, *16*, 846. [[CrossRef](#)]
29. Qi, D.; Wang, X.; Cheng, Y.; Gong, R.; Li, B. Design and characterization of one-dimensional photonic crystals based on ZnS/Ge for infrared-visible compatible stealth applications. *Opt. Mater.* **2016**, *62*, 52–56. [[CrossRef](#)]
30. Deng, Z.; Su, Y.; Qin, W.; Wang, T.; Wang, X.; Gong, R. Nanostructured Ge/ZnS films for multispectral camouflage with low visibility and low thermal emission. *ACS Appl. Nano Mater.* **2022**, *5*, 5119–5127. [[CrossRef](#)]
31. Kang, Q.; Li, D.; Wang, W.; Guo, K.; Guo, Z. Multiband tunable thermal camouflage compatible with laser camouflage based on GST plasmonic metamaterial. *J. Phys. D Appl. Phys.* **2021**, *55*, 065103. [[CrossRef](#)]
32. Wang, L.; Yang, Y.; Tang, X.; Li, B.; Hu, Y.; Zhu, Y.; Yang, H. Combined multi-band infrared camouflage and thermal management via a simple multilayer structure design. *Opt. Lett.* **2021**, *46*, 5224–5227. [[CrossRef](#)] [[PubMed](#)]
33. Peng, L.; Liu, D.; Cheng, H.; Zhou, S.; Zu, M. A multilayer film based selective thermal emitter for infrared stealth technology. *Adv. Opt. Mater.* **2018**, *6*, 1801006. [[CrossRef](#)]
34. Yang, M.; Zhou, M.; Yu, J.; Zhang, Y.; Xu, B.; Cheng, W.; Li, X. Infrared and Terahertz compatible absorber based on multilayer film. *Front. Phys.* **2021**, *9*, 633971. [[CrossRef](#)]
35. Zhu, H.; Li, Q.; Tao, C.; Hong, Y.; Xu, Z.; Shen, W.; Kaur, S.; Ghosh, P.; Qiu, M. Multispectral camouflage for infrared, visible, lasers and microwave with radiative cooling. *Nat. Commun.* **2021**, *12*, 1805. [[CrossRef](#)] [[PubMed](#)]
36. Pan, M.; Huang, Y.; Li, Q.; Luo, H.; Zhu, H.; Kaur, S.; Qiu, M. Multi-band middle-infrared-compatible camouflage with thermal management via simple photonic structures. *Nano Energy* **2020**, *69*, 104449. [[CrossRef](#)]
37. Luo, P.; Lan, G.; Nong, J.; Zhang, X.; Xu, T.; Wei, W. Broadband coherent perfect absorption employing an inverse-designed metasurface via genetic algorithm. *Opt. Express* **2022**, *30*, 34429–34440. [[CrossRef](#)]
38. Cai, H.; Sun, Y.; Wang, X.; Zhan, S. Design of an ultra-broadband near-perfect bilayer grating metamaterial absorber based on genetic algorithm. *Opt. Express* **2020**, *28*, 15347–15359. [[CrossRef](#)]
39. Liu, Q.; Sandgren, E.; Barnhart, M.; Zhu, R.; Huang, G. Photonic nanostructures design and optimization for solar cell application. *Photonics* **2015**, *2*, 893–905. [[CrossRef](#)]
40. You, P.; Li, X.; Huang, Y.; Ma, X.; Pu, M.; Guo, Y.; Luo, X. High-performance multilayer radiative cooling films designed with flexible hybrid optimization strategy. *Materials* **2020**, *13*, 2885. [[CrossRef](#)]
41. Andrea, S.; Paolo, B. Computation of the alpha cabin sound absorption coefficient by using the finite transfer matrix method(FTMM): Inter-laboratory test on porous media. *ASME J. Vib. Acoust* **2021**, *143*, 12–21.
42. Byrnes, S.J. Multilayer optical calculations. *arXiv* **2016**, arXiv:1603.02720. [[CrossRef](#)]
43. Generalized  $4 \times 4$  Matrix Algorithm for Light Propagation in Anisotropic Stratified Media (MATLAB Files). Available online: <https://zenodo.org/record/847015> (accessed on 8 January 2023).
44. Burnett, J.H.; Kaplan, S.G.; Stover, E.; Phenis, A. Refractive index measurements of Ge. In Proceedings of the Infrared Sensors, Devices, and Applications VI, San Diego, CA, USA, 20 September 2016.
45. Shkondin, E.; Takayama, O.; Panah, M.A.; Liu, P.; Larsen, P.V.; Mar, M.D.; Jensen, F.; Lavrinenko, A. Large-scale high aspect ratio Al-doped ZnO nanopillars arrays as anisotropic metamaterials. *Opt. Mater. Express* **2017**, *7*, 1606–1627. [[CrossRef](#)]
46. Yang, H.U.; D'Archangel, J.; Sundheimer, M.L.; Tucker, E.; Boreman, G.D.; Raschke, M.B. Optical dielectric function of silver. *Phys. Rev. B* **2015**, *91*, 235137. [[CrossRef](#)]
47. Rakić, A.D.; Djurišić, A.B.; Elazar, J.M.; Majewski, M.L. Optical properties of metallic films for vertical-cavity optoelectronic devices. *Appl. Opt.* **1998**, *37*, 5271–5283. [[CrossRef](#)] [[PubMed](#)]
48. Chen, Y.B.; Zhang, Z. Design of tungsten complex gratings for thermophotovoltaic radiators. *Opt. Commun.* **2007**, *269*, 411–417. [[CrossRef](#)]

49. Zhao, J.; Zhang, Z. Electromagnetic energy storage and power dissipation in nanostructures. *J. Quant. Spectrosc. Radiat. Transf.* **2015**, *151*, 49–57. [[CrossRef](#)]
50. Liu, Y.; Jin, R.; Qiu, J.; Liu, L. Spectral radiative properties of a nickel porous microstructure and magnetic polariton resonance for light trapping. *Int. J. Heat Mass Transf.* **2016**, *98*, 833–844. [[CrossRef](#)]
51. S4: Stanford Stratified Structure Solver. Available online: <https://github.com/victorliu/S4> (accessed on 10 February 2023).

**Disclaimer/Publisher’s Note:** The statements, opinions and data contained in all publications are solely those of the individual author(s) and contributor(s) and not of MDPI and/or the editor(s). MDPI and/or the editor(s) disclaim responsibility for any injury to people or property resulting from any ideas, methods, instructions or products referred to in the content.